Electrochimica Acta 321 (2019) 134723

Contents lists available at ScienceDirect

Electrochimica Acta

journal homepage: www.elsevier.com/locate/electacta

Amorphous and crystalline TiO_2 nanoparticle negative electrodes for sodium-ion batteries

Changjian Deng [a], Chunrong Ma [a], Miu Lun Lau [a], Paige Skinner [a], Yuzi Liu [b], Wenqian Xu [c], Hua Zhou [c], Yang Ren [c], Yadong Yin [d], Bethany Williford [a], Michael Dahl [a, d], Hui (Claire) Xiong [a, *]

[a] Micron School of Materials Science and Engineering, Boise State University, Boise, ID, 83725, USA
[b] Center for Nanoscale Materials, Argonne National Laboratory, Lemont, IL, 60439, USA
[c] X-ray Science Division, Argonne National Laboratory, Lemont, IL, 60439, USA
[d] Department of Chemistry, University of California Riverside, Riverside, CA, 92521, USA

ARTICLE INFO

Article history:
Received 12 June 2019
Received in revised form
13 August 2019
Accepted 18 August 2019
Available online 19 August 2019

Keywords:
TiO_2
Amorphous
Crystalline
Nanoparticles
Sodium ion batteries

ABSTRACT

Titanium dioxide (TiO_2) is a promising negative electrode for sodium ion batteries (SIBs). Although TiO_2 materials with amorphous (A-TiO_2) and single-phase crystalline structures (C−TiO_2) have been *separately* explored, the study to compare the fundamental electrochemistry of A-TiO_2 and C−TiO_2 is limited. In this work, we investigated A-TiO_2 and C−TiO_2 nanoparticles with identical chemical composition and morphology. C−TiO_2 exhibits enhanced electrochemical performance than A-TiO_2 in terms of rate capability and cycle life. Cyclic voltammetry (CV) analysis suggests reversible Na ion insertion/extraction in C−TiO_2. However, such process is irreversible in the case of A-TiO_2. The charge storage mechanisms in both samples were studied to show that diffusion-controlled intercalation process becomes significant in C−TiO_2 sample. The C−TiO_2 sample has a better Na^+ diffusivity measured through the galvanostatic intermittent titration technique (GITT) compared to A-TiO_2, which corroborates well with the rate capability study. Furthermore, the evolution of local structure of the TiO_2 samples was analyzed by *ex situ* pair distribution function (PDF) to understand the variation in electrochemical properties. It reveals that the corner-shared Ti−Ti distance along Na ion diffusion pathway increases with the increase of crystallinity, leading to the expanded diffusion channels and therefore more active sites and faster diffusion.

1. Introduction

Sodium ion batteries (SIB) are attractive alternatives to lithium ion batteries due to the abundant sodium resources and the utilization of aluminum current collector for negative electrodes, leading to reduced cost and making it particularly promising for large-scale energy storage systems [1–4]. Nevertheless, graphite that has been widely used as the most popular negative electrode material for lithium ion batteries is not suitable with conventional Na electrolytes due to the instability of Na-graphite intercalation compound formation [5]. Therefore, efforts have been made to search for new negative electrode materials for SIB. Hard carbon has been intensively studied but the low intercalation voltages (0−0.1 V vs Na/Na^+) is close to that of sodium plating, which could lead to dendrite formation and unsafe operation [6]. Alloy-type anodes including P, Sn and Sb, possess high theoretical capacities but suffer from large volume changes which leads to poor cycling performance [7–9]. Organic materials are also investigated as the negative electrode materials for SIB, however, they have issues with poor electronic conductivity and dissolution in the organic electrolyte [10,11].

Titanium dioxide (TiO_2) is a promising negative electrode material due to the safe operation voltage, structural stability during cycling, and acceptable electronic conductivity [12]. Amorphous [13], anatase [14–18], bronze [19], and rutile [20] TiO_2 materials have been studied for SIB. Xiong et al. directly grew amorphous anodic TiO_2 nanotubes on the Ti current collector without binders and additives, and the electrochemical performance was evaluated within a sodium half-cell. The amorphous TiO_2 nanotube electrode exhibits a capacity of 150 mAh g^{-1} at 0.05 A g^{-1} [13]. Wu et al. prepared anatase TiO_2 nanoparticles for high-power sodium ion

* Corresponding author.
E-mail address: clairexiong@boisestate.edu (H. Xiong).

https://doi.org/10.1016/j.electacta.2019.134723
0013-4686/

batteries, where 100 mAh g^{-1} at 5.5C was obtained after 1000 cycles without significant capacity decay [14]. Furthermore, they investigated the sodium ion insertion process and proposed a new reaction mechanism that sodium ion insertion partially reduces the stable titanium oxide and forms metallic titanium, sodium oxide, and amorphous sodium titanate [15]. The newly-formed amorphous sodium titanate contributes to the most of the reversible capacity [15]. Moreover, Li et al. investigated the sodium insertion/extraction mechanism in anatase TiO_2, where sodium ion insertion leads to the phase transition from anatase ($I4_1/amd$) to layered Na_xTiO_2 (R-3m) with high degree of disorder, and the local structure of the anatase was recovered with short-range order after sodium extraction [16]. Zhang et al. reported a hierarchical porous anatase TiO_2 anode from an iso-polyoxotitanate cluster, showing great rate capability [21]. Huang et al. reported TiO_2(B) nanotubes with a 50 mAh g^{-1} capacity after 90 cycles and identified that the sodium insertion along (001) interlayer plane [19]. Gu et al. prepared hierarchical tubular rutile TiO_2 nanorods with a high reversible capacity of 79 mAh g^{-1} at 0.3C after 1000 cycles [20].

Although TiO_2 materials with various crystalline structures and morphologies have been studied by different research groups, the study to compare Na ion storage in amorphous and crystalline TiO_2 materials with identical chemical composition and morphology is limited. Su et al. compared the electrochemical performance of amorphous, mixed anatase/rutile and pure anatase TiO_2 hollow nanospheres in SIB [22]. However, the amorphous TiO_2 is deposited on the carbon hollow spheres that makes the chemical composition different from the pure anatase one. Bella et al. investigated the Na storage in amorphous and crystalline TiO_2 nanotubes [23]. Although both amorphous and anatase nanotubes are composed of TiO_2, the morphology of amorphous nanotubes is different as the anatase TiO_2 nanotubes exhibit increase in wall roughness and the walls become thinner going from the bottom to the top of the array [23]. It has been reported that the behavior of Na ion storage is largely dependent on the morphology of the host materials [24]. In terms of TiO_2 materials particularly, the electronic [25], mechanic [26], catalytic [27], thermal [28] properties as well as alkali ion storage [29] are closely related to the morphology of the materials. Zero-dimensional solid nanoparticles provide short diffusion pathway from the core to the surface [30]. Moreover, solid rather than hollow geometry is assumed to offer higher volumetric energy density in theory. Therefore, in addition to hollow nanospheres [22] and one-dimensional nanotubes [23], it is also necessary to investigate the effect of crystallinity on solid TiO_2 nanoparticles for sodium-ion batteries.

Herein, we report a study of crystallinity effect on electrochemical charge storage properties of mesoporous TiO_2 nanoparticles as a negative electrode for SIB. We have prepared amorphous (A-TiO_2) and crystalline (C−TiO_2) anatase TiO_2 nanospheres with identical chemical composition and particle size (i.e., ~200 nm) for the investigation. The crystallinity was characterized by X-ray diffraction (XRD), Raman spectroscopy and transmission electron spectroscopy (TEM), respectively. A-TiO_2 sample demonstrates a sloping characteristic in voltage profile during charging and discharging processes, indicative of a single solid solution behavior. On the other hand, C−TiO_2 sample exhibits plateaus upon discharging and a sloping curve on the charging process during the first cycle, suggesting the irreversible phase transition during Na ion insertion [15]. The electrochemical performance in terms of rate capability and cycle life directly relates to the crystallinity of the materials, where crystalline TiO_2 exhibits higher capacity. Cyclic voltammetry (CV) with varying scan rates was conducted to understand the Na ion charge storage mechanism. It is suggested that the diffusion-controlled intercalation process becomes significant in C−TiO_2 sample. Results from the galvanostatic intermittent titration technique (GITT) suggest that the C−TiO_2 sample has a better Na^+ diffusivity compared to A-TiO_2, which corroborates well with the rate capability study. Furthermore, the local structure of the TiO_2 samples was analyzed by *ex situ* pair distribution function (PDF), which shows that the corner-shared Ti−Ti distance along Na ion diffusion pathway increases with the increase of crystallinity, leading to the expanded diffusion channels and therefore more active sites and faster diffusion. Our study provides guidance toward the design rules for electrode materials with the same composition but tunable crystallinity for improved electrochemical performance for different applications in SIBs.

2. Experimental section

2.1. Synthesis

A-TiO_2 and C−TiO_2 samples were prepared by the water-assisted sol-gel method reported previously [31]. In brief, 0.85 mL of tetrabutyl orthotitanate (TBOT) was added to a mixture of 50 mL of 200-proof ethanol, 0.15 g of hydroxypropyl cellulose (HPC) and 300 μL of sodium chloride (0.04 M). After stirring in air for 3 h, the precipitate was obtained by centrifuging and was washed several times by both 200-proof ethanol and de-ionized (DI) water. The product was well-dispersed in a mixture of 19 mL of DI water and 1 mL of NaF solution (1 mg/10 mL) by sonication. Subsequently, the solution was stirred and heated for 30 min at the temperature of 50 °C and 100 °C for the A-TiO_2 and C−TiO_2, respectively. The samples were washed with 200-proof ethanol and de-ionized (DI) water and dried.

2.2. Material characterization

XRD was conducted by Rigaku Miniflex 600 with Cu-Kα radiation (λ = 1.5418 Å), at a scan rate of 0.05°/s in the 2θ range of 20−80°. Raman spectroscopy was obtained by a Horiba Scientific Lab RAM HR Evolution spectrometer using the 442 nm He:Cd laser with signal accumulations of three 30s scans. The incident laser power was 100 mW, and samples were viewed at a magnification of 100×. TEM characterizations were performed by FEI Titan 80−300 ST at the accelerating voltage of 200 kV. The surface area of TiO_2 materials is measured by nitrogen gas adsorption and desorption isotherms by a NOVA 3200e Quantachrome surface and pore size analyzer and calculated by the standard multipoint Brunauer-Emmett-Teller (BET) method. *Ex situ* PDF was conducted by Synchrotron X-ray with the wavelength of 0.24128 Å at beamline 17-BM of the Advanced Photon Source in Argonne National Laboratory. The pristine and cycled samples were sealed with Kapton tape. The data was collected by a PerkinElmer amorphous silicon detector in transition mode. The collected 2D diffraction data were integrated into 1D diffraction intensity versus 2θ through program GSAS-II [32]. The 1D data in reciprocal space was subsequently converted to PDF profiles with program PDFgetX3 [33].

2.3. Electrochemical characterization

The electrochemical performance of TiO_2 samples was evaluated in coin-type half cells. The cells were assembled in an argon filled glovebox ([O_2]<0.5 ppm) using glassy fiber as the separator, 1 M sodium perchlorate ($NaClO_4$) in propylene carbonate (PC) as the electrolyte, metallic sodium as the counter electrode and laminated electrodes as the working electrode. The laminated electrodes are composed of 80% of TiO_2 active materials, 10% of super carbon C45 (Timcal America Inc.) and 10% of sodium carboxymethylcellulose (CMC, Dow Chemical Company). The coin cells were tested with a potential window of 0.1−2 V in an Arbin battery tester. Cyclic

voltammograms were recorded in three-electrode cells (EL Cell, ECC-REF) with the potential window from 0.1 to 2 V at varying scan rates of 0.1–10 mV s^{-1}. GITT was conducted in a three-electrode cell (ECC-Ref. EL-CELL) between 0.1 and 2 V at a current rate of 10 mA g^{-1} for a 30-min pulse followed by a rest period of 12 h to approach the steady-state value.

3. Results and discussion

3.1. Materials characterization

The structures of TiO_2 samples are identified by XRD (Fig. 1a). There are no pronounced peaks in the XRD of the A-TiO_2 sample, suggesting its amorphous structure. C–TiO_2 sample exhibits broad characteristic peaks due to its nanoscale crystallite size, which can be indexed as the anatase phase (space group: $I4_1/amd$) [34]. The crystallite size calculated by Scherrer's equation [35] is 4.7 nm.

Raman spectroscopy as a local probe is very sensitive to the crystallinity of materials where the scatterings become weak and the corresponding peaks become broad when the sample has local lattice imperfections [36]. The Raman spectra of TiO_2 samples are shown in Fig. 1b. Anatase TiO_2 has a tetragonal structure (space group $I4_1/amd$) and is comprised of two TiO_2 units per primitive cell, leading to six Raman active modes in the vibrational spectrum:

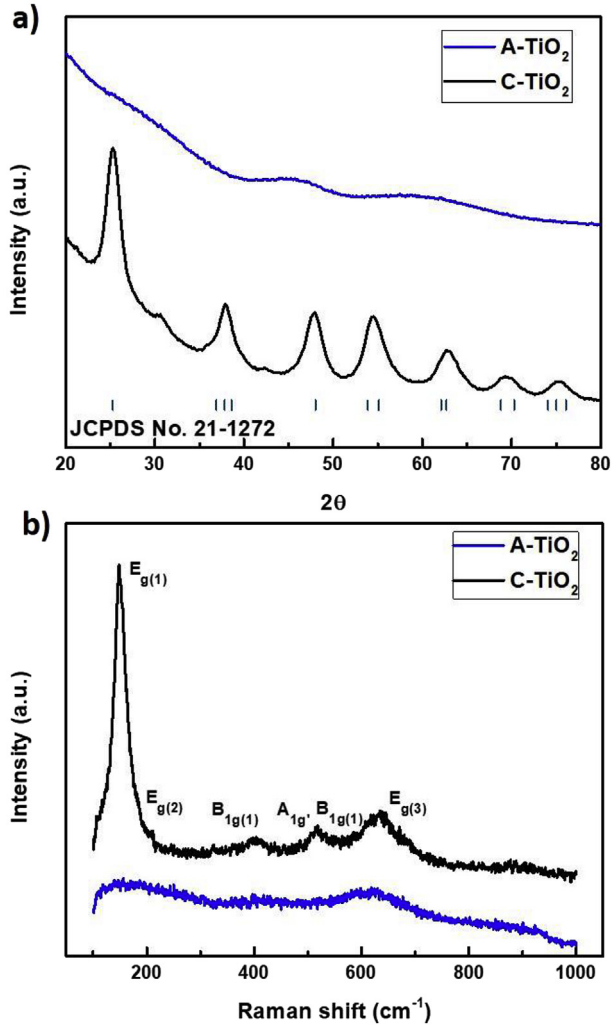

Fig. 1. (a) XRD and (b) Raman spectra of pristine TiO_2 nanoparticle samples.

three E_g modes centered around 144, 196, 639 cm^{-1} ($E_{g(1)}$, $E_{g(2)}$ and $E_{g(3)}$, respectively), two B_{1g} modes centered around 397 and 519 cm^{-1} ($B_{1g(1)}$, and $B_{1g(2)}$, respectively), and an A_{1g} mode at 513 cm^{-1} [37]. The Raman spectra of A-TiO_2 shows no distinct peaks, which suggests that the structure is amorphous. As for C–TiO_2 sample, the intensity of the $E_{g(1)}$ peak (148 cm^{-1}) significantly increases and the high-frequency peaks become pronounced, suggesting the highly-crystalline structure.

The morphology and structure of TiO_2 nanoparticle samples are further investigated by TEM. Despite of different crystallinity, A-TiO_2 (Fig. 2a) and C–TiO_2 (Fig. 2b) samples are composed of spherical nanoparticles with similar particle size, approximately 200 nm, consistent with our previous study [31]. The degree of ordering of the samples are examined by high resolution TEM (HRTEM) and selected area electron diffraction (SAED). The lack of pronounced lattice fringes (Fig. 2c) and the characteristic diffusive ring in SAED (Fig. 2e) suggest that the A-TiO_2 sample is amorphous. For the C–TiO_2 sample, the HRTEM image is composed of lattice fringes of anatase (101) planes where the d-spacing is 3.51 Å (Fig. 2d), and the SAED pattern shows well-defined and pronounced diffraction rings attributed to anatase structure (Fig. 2f), both of which indicate the highly-crystalline anatase structure of C–TiO_2 sample. The morphology and crystallinity of TiO_2 samples are also investigated after 20 cycles by TEM (Fig. S1, Supporting Information). The results suggest that both A-TiO_2 (Fig. S1a) and C–TiO_2 (Fig. S1b) maintained spherical morphology. In addition, A-TiO_2 (Fig. S1c) and C–TiO_2 (Fig. S1d) remained amorphous and anatase phase after cycling, respectively.

3.2. Electrochemical performance

The electrochemical performance of TiO_2 samples is shown in Fig. 3. The voltage profiles of the first and 20th cycle at the rate of 20 mA g^{-1} with the potential window of 0.1–2.0 V is shown in Fig. 3a. At the first cycle, A-TiO_2 sample exhibits sloping feature on both charging and discharging curves, suggesting Na ion diffusion through single solid solution. However, C–TiO_2 sample has a small plateau at 0.40 V on the discharging curve, suggesting the possible phase transition of the metastable sodium titanate phase further into metallic titanium, sodium superoxide and amorphous sodium titanate phase [15]. A slightly different plateau voltage is found in comparison to the reported one (0.3 V), which possibly is associated with the variation in particle size and/or defects of the sample [38]. The small plateau is absent in the charge curve, suggesting irreversible phase transformation in C–TiO_2 during the first discharging process, consistent with a previous study [15]. The first cycle Coulombic efficiency (CE) of A-TiO_2 and C–TiO_2 is 27% and 47%, respectively. The low first cycle CE of both samples is possibly related to the formation of solid electrolyte interphase (SEI) [39], irreversible phase transformation in TiO_2 [15], electrolyte decomposition, as well as side reactions. At the 20th cycle, the Coulombic efficiency of A-TiO_2 and C–TiO_2 samples increases to 98% and 94% with the reversible capacity of 65 and 124 mAh g^{-1}, respectively. The rate capability of the samples is evaluated and presented using the discharge capacity (Fig. 3b) at the current rate of 0.02 A g^{-1}, 0.1 A g^{-1}, and 0.5 A g^{-1}, respectively. The reversible capacity at 0.02 A g^{-1} of A-TiO_2 and C–TiO_2 sample is 65 mAh g^{-1} and 124 mAh g^{-1}, respectively. The capacity moderately drops with the increase of current rates. At the high rate of 0.5 A g^{-1}, the A-TiO_2, and C–TiO_2 sample delivers 26 mAh g^{-1} and 76 mAh g^{-1}, respectively. When the current rate is ramped back to 0.02 A g^{-1}, the capacity of the A-TiO_2 and C–TiO_2 sample recovers to 59 mAh $g^{-1}$and 112 mAh g^{-1}, suggesting good capacity retention and rate capability. Moreover, the cycle life performance at the rate of 100 mA g^{-1} of the samples is shown in Fig. 3c. The A-TiO_2 and C–TiO_2 sample deliver reversible

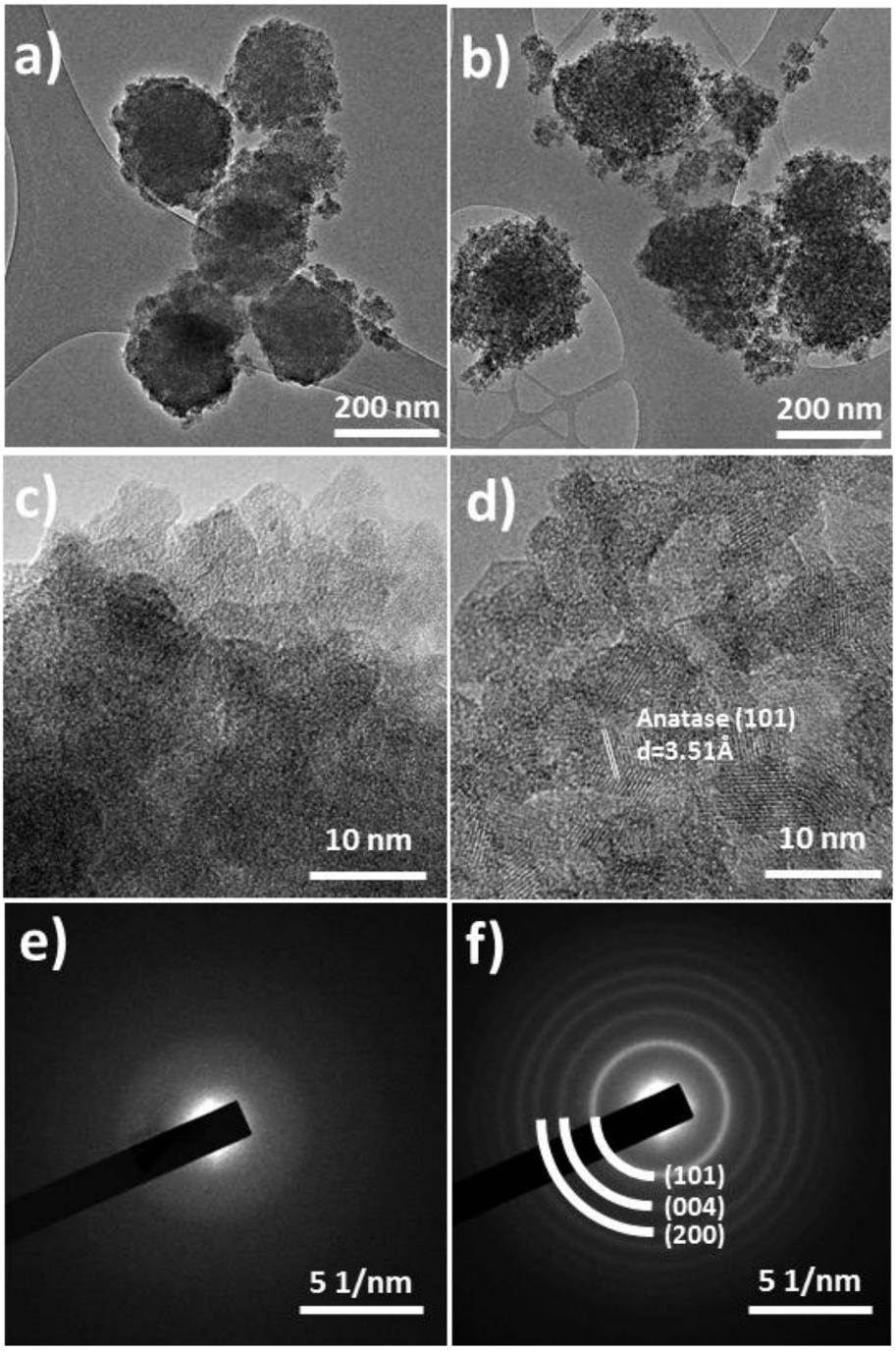

Fig. 2. TEM images of (a) A-TiO_2 and (b) C−TiO_2; HRTEM images of (c) A-TiO_2 and (d) C−TiO_2; SAED patterns of (e) A-TiO_2 and (f) C−TiO_2.

capacity of 50 mAh g^{-1} and 99 mAh g^{-1} after 100 cycles, respectively. Note that both rate capability and cycle life study show that the C−TiO_2 electrode performs much better than that of the A-TiO_2 sample, suggesting the electrochemical properties of TiO_2 nanoparticle electrode are related to the crystallinity of the materials.

3.3. Electrochemical charge storage and transport mechanisms

CV is conducted to understand the sodium insertion and extraction in TiO_2 nanoparticle samples. Fig. 4a shows the CV curves of TiO_2 samples at the rate of 0.2 mV s^{-1} after 3 pre-cycles. The C−TiO_2 sample shows a broad redox pair where the reduction and oxidation peak is located at 0.60 V and 0.83 V, respectively. On the other hand, there is an irreversible reduction peak of the A-TiO_2 sample located at 0.88 V, suggesting the irreversible sodium insertion into the A-TiO_2 host structure. It indicates the sodium ions are trapped in the A-TiO_2 sample, which possibly leads to a lower specific capacity and Coulombic efficiency than the C−TiO_2 sample. The voltammetry with various scan rates of 0.1, 0.2, 0.5, 1 and 2 mV s^{-1} of A-TiO_2 and C−TiO_2 sample are shown in Fig. 4c and (d), respectively to investigate the charge storage mechanism, which can be analyzed according to the power law relationship [40–42]:

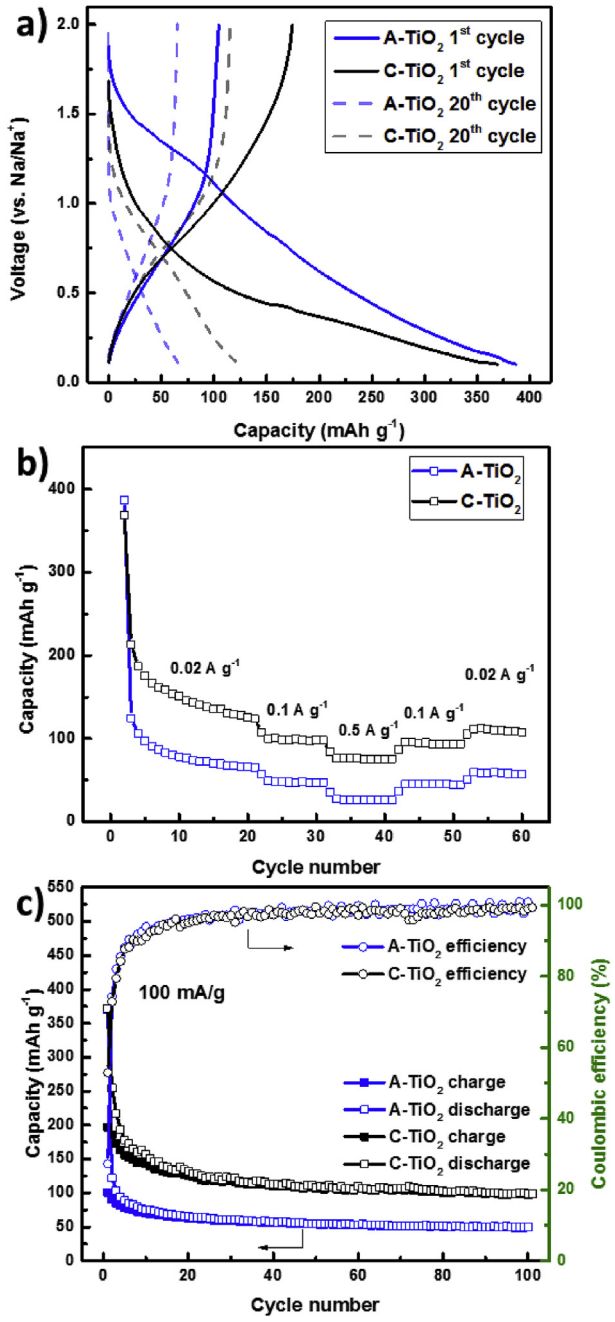

Fig. 3. Electrochemical properties of the TiO_2 nanoparticle electrodes: (a) voltage profile, (b) rate capability and (c) cycle life performance of TiO_2 samples. The voltage window for all of galvanic testing is 0.1–2.0 V.

$$i = av^b \tag{1}$$

Where i is the observed current, v as the scan rate, a and b as the adjustable parameters. The b-values of 0.5 and 1 represent that the charge storage is limited by diffusion controlled intercalation and capacitive processes, respectively [40,41]. The b-values vs. voltage plots of TiO_2 samples during the discharging process are shown in Fig. 4b. The b-values of A-TiO_2 sample are in general larger than that of C—TiO_2 sample throughout the whole discharging process, suggesting the amorphous component in the structure leads to the increase of capacitive contribution. As for C—TiO_2 sample, the b-values are larger than 0.9 when discharge potentials are above 0.8 V, suggesting a significantly capacitive-controlled process when less Na ions are incorporated [15]. When discharged below 0.8 V, the b-values of C—TiO_2 sample continuously decrease, suggesting a gradual transition from a capacitive-limiting mechanism to mixed contributions by diffusion [15] and surface capacitive processes.

In addition, the charge storage can be quantitatively determined by the following equation:

$$i(V) = k_1 v + k_2 v^{1/2} \tag{2}$$

where $k_1 v$ and $k_2 v^{1/2}$ represent the capacitive contribution and diffusion-controlled intercalation respectively [40,43]. Therefore, we are able to quantitatively investigate the charge storage mechanism by the fraction of $k_1 v$ and $k_2 v^{1/2}$. Fig. 4d and (f) demonstrated the CV curve of A-TiO_2 and C—TiO_2 sample at a slow scan rate of 0.1 mV s^{-1}, respectively, where the shaded area indicated the capacitive contribution to the charge storage. The capacitive contribution of A-TiO_2 and C—TiO_2 sample is 57% and 45%, respectively. More than half of the charge storage is comprised of the capacitive contribution in the A-TiO_2 sample. However, the contribution from the diffusion controlled intercalation is more significant than the capacitive contribution in C—TiO_2 sample. The BET surface area of A-TiO_2 and C—TiO_2 sample are 385 and 251 m^2 g^{-1}, respectively, comparable to the reported TiO_2 nanoscale materials (Table S1, Supporting Information). The larger surface area in A-TiO_2 sample leads to higher capacitive contribution.

We conducted GITT of TiO_2 samples (Fig. 5a) to quantitatively investigate the Na^+ diffusivity in the TiO_2 samples (details of the GITT analysis can be found in the Supporting Information). The log plot of the sodium ion diffusivity in the insertion process as a function of voltage is shown in Fig. 5b. The Na^+ diffusivity of the C—TiO_2 sample gradually decreases with the sodium insertion process from 1.2 V to 0.4 V, possibly because the sodium insertion leads to the sluggish formation of a metastable sodium titanate phase and subsequent solid state sodium diffusion [15]. When cycled below 0.4 V, the diffusivity of the C—TiO_2 sample slightly increased due to the formation of the amorphous sodium titanate phase [15] where the disordered structure with defects could offer active sites and spatial channels for the sodium diffusion [13]. In terms of A-TiO_2 sample, the diffusivity gradually decreased from 0.88 V to 0.28 V, possibly due to the limited access to active sites with the continuous insertion of sodium ions. It is worth noting that the diffusivity of C—TiO_2 sample is higher than that of A-TiO_2 sample across the whole voltage window, consistent with the results from rate study.

3.4. Local structural evolution of TiO_2 nanoparticle samples

In addition to electrochemical characterizations, *ex situ* PDF was conducted to investigate the structural evolution of the TiO_2 samples. Although XRD has been successfully applied to investigate the crystalline structure of materials for decades, it has limits to characterize nanoscale crystallites and highly-disordered structures [44]. The PDF technique, however, reveals the short- and intermediate-range order of the materials, offering a new opportunity to investigate disordered and partially ordered materials [45]. The PDF results of TiO_2 samples at the pristine state are shown in Fig. 6a. The intensity in PDF damps at approximately 8 Å and 48 Å for A-TiO_2, and C—TiO_2 samples, respectively, suggesting the increased ordering with the increase of crystallinity. Moreover, the stronger amplitude of C—TiO_2 sample also indicates better-defined crystallinity than that of A-TiO_2 sample in short-range ordering region. The *ex situ* local atomic feature is presented in Fig. 6b in the low real-space region (1.5 Å –9 Å), where 1st discharged and 1st charged samples are plotted together to understand the structural

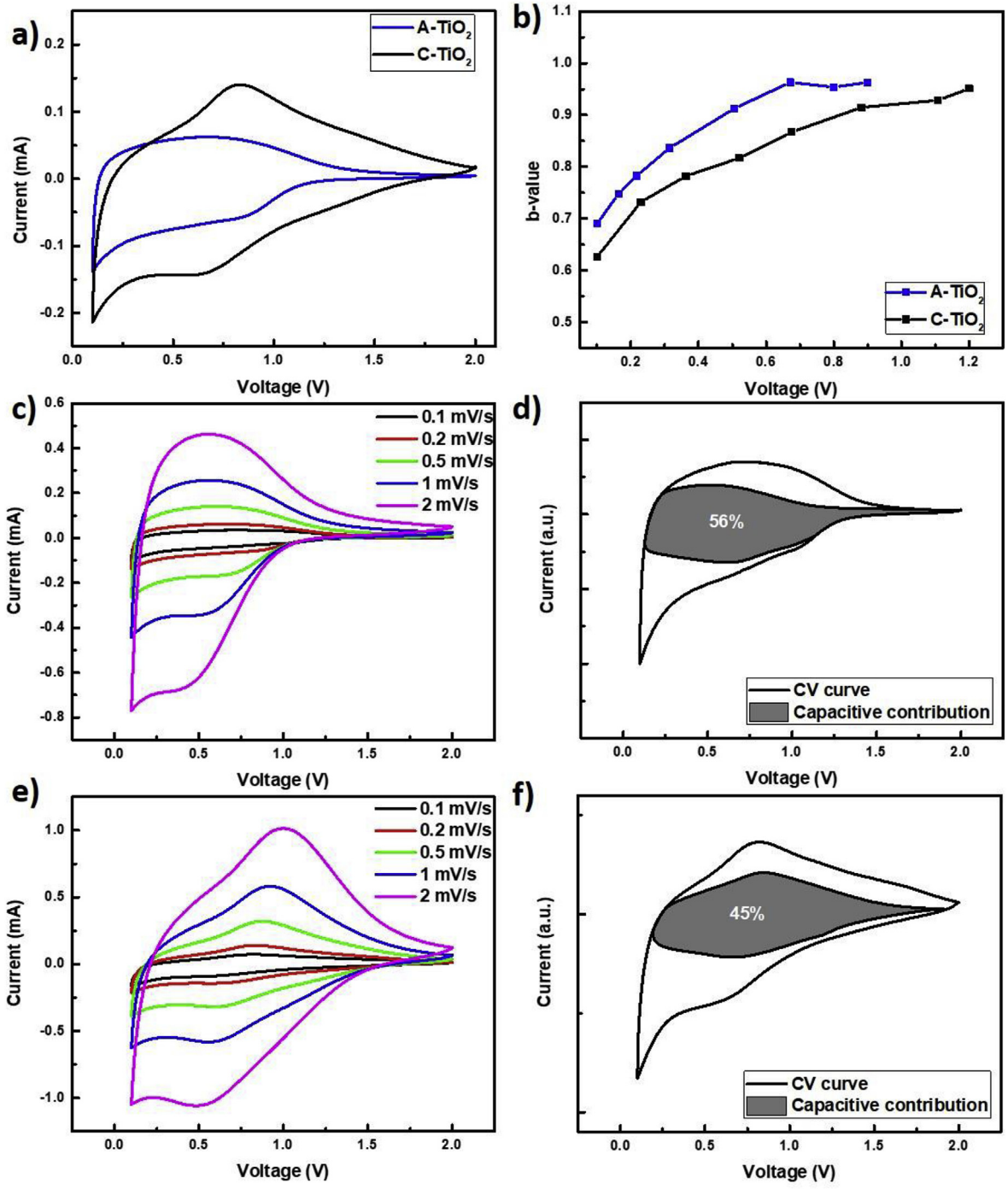

Fig. 4. (a) CV curves of TiO_2 samples at the scan rate of 0.2 mV s^{-1} with the voltage window of 0.1–2.0 V; (b) The *b*-value of TiO_2 samples; and the CV curves of (c) A-TiO_2 and (e) C–TiO_2 at various scan rates; The charge storage mechanism of (d) A-TiO_2 and (f) C–TiO_2 samples at the rate of 0.1 mV s^{-1}.

evolution during cycling. After the 1st cycle, both TiO_2 samples show a weakened amplitude, suggesting decreased ordering after Na ion (de)insertion process. The peaks in the pristine TiO_2 samples at 1.93 Å, 2.51 Å, 3.01 Å and 3.75 Å can be indexed to the Ti–O, O–O, Ti–Ti bond distance, respectively [16,46]. At the 1st discharged state where Na ions are inserted, the distinct O–O peak becomes a subtle shoulder (2.41 Å), which can be assigned to the newly-formed Na–O bond [16], suggesting the declined O–O ordering. Such change is possibly due to the phase transition from anatase TiO_2 (space group: $I4_1/amd$) to layered Na_xTiO_2 (space group: R-3m) where cationic mixing and vacancies were initiated after Na insertion [16]. The O–O ordering does not recover after Na ions are extracted (1st charged state), suggesting the irreversible Na ion insertion process. The unit cell of anatase TiO_2 crystal structure is shown in Fig. 6c where black and red balls indicate Ti atoms and O atoms, respectively. It has been reported that the active sites for Na ion insertion are the empty tetrahedral and octahedral sites along the zigzag TiO_6 channel [47,48]. The channel for sodium diffusion is directly related to the Ti–Ti distance in corner-sharing TiO_6 octahedra (highlighted in dashed purple lines in Fig. 6b and c. The Ti–Ti

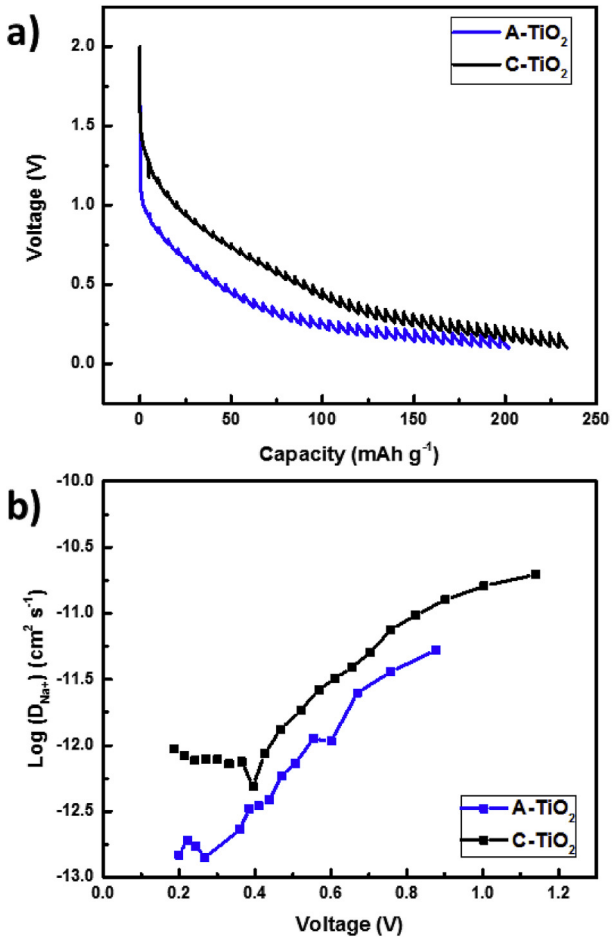

Fig. 5. (a) GITT profiles and (b) Log diffusivity vs. voltage during discharge process of TiO_2 samples.

distance of A-TiO_2 and C—TiO_2 samples is 3.75 Å and 3.85 Å, which increases with the increase of crystallinity. Because the large Ti—Ti distance offers more active sites and expanded zigzag channels for Na ion diffusion, C—TiO_2 sample with larger Ti—Ti distance exhibits the higher specific capacity and enhanced rate capability than the A-TiO_2 sample. Though the Ti—Ti distance decreased for both TiO_2 samples after Na ion insertion and/or extraction process due to the irreversible phase transition, C—TiO_2 sample demonstrates strong amplitudes and well-defined peaks, suggesting greater Ti—Ti ordering which possibly contributes to its better Na^+ diffusivity compared to A-TiO_2 sample.

4. Conclusions

Amorphous and highly-crystalline TiO_2 nanoparticles were successfully prepared by a sol-gel process with different heat treatments. The uniform particle size distribution of all TiO_2 samples was confirmed by TEM images. The amorphous and crystalline features were confirmed at bulk, molecular, and atomic scale by XRD, Raman spectroscopy, TEM, PDF, respectively. The increase of crystallinity leads to better electrochemical performance in terms of Coulombic efficiency, rate capability and cycle life. An irreversible Na insertion process of A-TiO_2 sample is indicated in CV, which is possibly associated with its lower specific capacity and Coulombic efficiency compared to that of the C—TiO_2 sample. The Na ion diffusion coefficient was evaluated by GITT where more crystallinity led to a larger diffusion coefficient. The charge storage

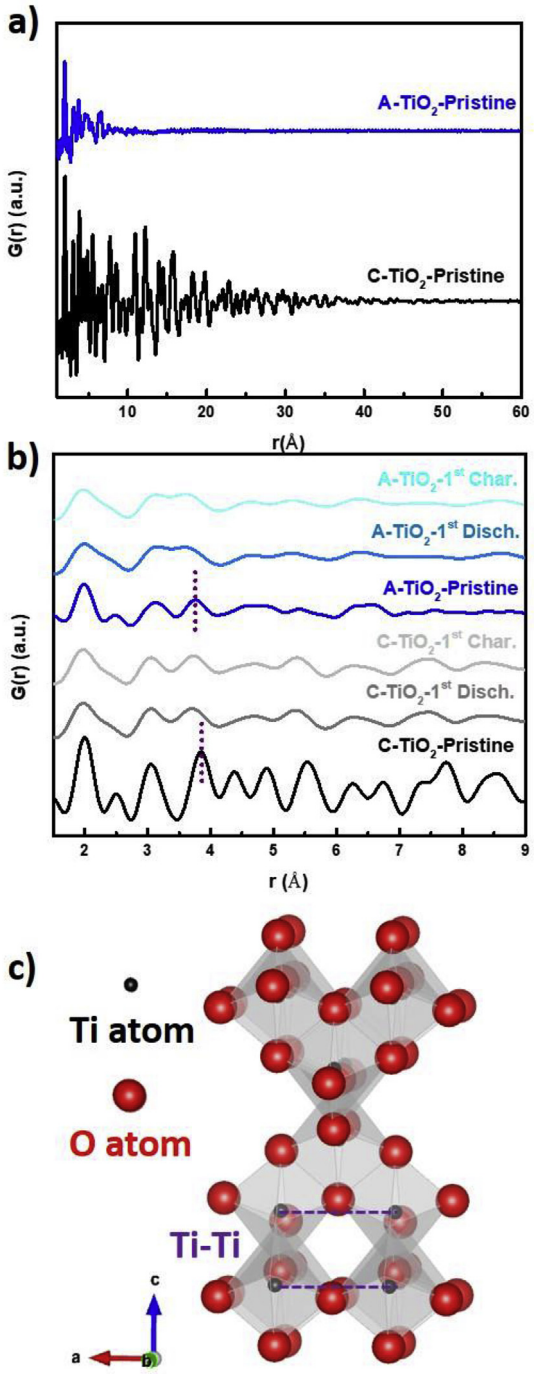

Fig. 6. (a) The PDF curves of pristine, 1st charged and 1st discharged TiO_2 samples with the atomic distance ranged from 1 to 60 Å.; (b) The pristine, 1st charged and 1st discharged PDF curves of TiO_2 samples with the enlarged range of 1 Å −9 Å. The purple line illustrated the corner-shared Ti—Ti distance. (c) The scheme of crystal structure of anatase TiO_2. The purple dashed line represents Ti—Ti in corner-sharing TiO_6 octahedral distances. (For interpretation of the references to colour in this figure legend, the reader is referred to the Web version of this article.)

mechanism of the TiO_2 nanoparticle samples were evaluated by CV with varying scan rates. It was found that A-TiO_2 sample has higher capacitive contribution compared to the C—TiO_2 sample. In addition to electrochemical evaluation, PDF was conducted to understand the local structural evolution of the TiO_2 nanoparticle samples upon cycling. The Na ion diffusion pathway was evaluated by the corner-shared Ti—Ti distance, which increased with the

increase of crystallinity. The increased Ti—Ti distance in C—TiO_2 sample leads to larger diffusion channels, more active sites and faster Na ion diffusion than the A-TiO_2 sample. Although the Ti—Ti distance decreases for both TiO_2 samples after the Na ion insertion/extraction processes due to the irreversible phase transitions, C—TiO_2 sample exhibits strong amplitude and well-defined peaks in PDF, suggesting better Ti—Ti ordering which possibly contributes to its higher capacity, great rate capability and cycling performance.

Conflicts of interest

The authors declare no competing financial interest.

Acknowledgements

The authors acknowledge support from the National Science Foundation under Grant No. DMR-1454984. Use of the Center for Nanoscale Materials, an Office of Science user facility, was supported by the U.S. Department of Energy, Office of Science, Office of Basic Energy Sciences, under Contract No. DE-AC02-06CH11357. This research used resources of the Advanced Photon Source, a U.S. Department of Energy (DOE) Office of Science User Facility operated for the DOE Office of Science by Argonne National Laboratory under Contract No. DE-AC02-06CH11357.

Appendix A. Supplementary data

Supplementary data to this article can be found online at https://doi.org/10.1016/j.electacta.2019.134723.

References

[1] N. Yabuuchi, K. Kubota, M. Dahbi, S. Komaba, Chem. Rev. 114 (2014) 11636—11682.
[2] H.L. Pan, Y.S. Hu, L.Q. Chen, Energy Environ. Sci. 6 (2013) 2338—2360.
[3] D. Kundu, E. Talaie, V. Duffort, L.F. Nazar, Angew. Chem. Int. Ed. 54 (2015) 3431—3448.
[4] D. Kim, E. Lee, M. Slater, W.Q. Lu, S. Rood, C.S. Johnson, Electrochem. Commun. 18 (2012) 66—69.
[5] G. Yoon, H. Kim, I. Park, K. Kang, Adv. Energy Mater 7 (2017) 1601519.
[6] D.A. Stevens, J.R. Dahn, J. Electrochem. Soc. 147 (2000) 1271—1273.
[7] J.F. Qian, X.Y. Wu, Y.L. Cao, X.P. Ai, H.X. Yang, Angew. Chem. Int. Ed. 52 (2013) 4633—4636.
[8] Y.H. Xu, Y.J. Zhu, Y.H. Liu, C.S. Wang, Adv. Energy Mater 3 (2013) 128—133.
[9] Y.J. Zhu, X.G. Han, Y.H. Xu, Y.H. Liu, S.Y. Zheng, K. Xu, L.B. Hu, C.S. Wang, ACS Nano 7 (2013) 6378—6386.
[10] Z.P. Song, H.S. Zhou, Energy Environ. Sci. 6 (2013) 2280—2301.
[11] Z.P. Song, Y.M. Qian, T. Zhang, M. Otani, H.S. Zhou, Adv. Sci. 2 (2015).
[12] S.H. Guo, J. Yi, Y. Sun, H.S. Zhou, Energy Environ. Sci. 9 (2016) 2978—3006.
[13] H. Xiong, M.D. Slater, M. Balasubramanian, C.S. Johnson, T. Rajh, J. Phys. Chem. Lett. 2 (2011) 2560—2565.
[14] L.M. Wu, D. Buchholz, D. Bresser, L.G. Chagas, S. Passerini, J. Power Sources 251 (2014) 379—385.
[15] L.M. Wu, D. Bresser, D. Buchholz, G.A. Giffin, C.R. Castro, A. Ochel, S. Passerini, Adv. Energy Mater 5 (2015).
[16] W. Li, M. Fukunishi, B.J. Morgan, O.J. Borkiewicz, K.W. Chapman, V. Pralong, A. Maignan, O.I. Lebedev, J.W. Ma, H. Groult, S. Komaba, D. Damboumet, Chem. Mater. 29 (2017) 1836—1844.
[17] S.T. Myung, N. Takahashi, S. Komaba, C.S. Yoon, Y.K. Sun, K. Amine, H. Yashiro, Adv. Funct. Mater. 21 (2011) 3231—3241.
[18] K.T. Kim, G. Ali, K.Y. Chung, C.S. Yoon, H. Yashiro, Y.K. Sun, J. Lu, K. Amine, S.T. Myung, Nano Lett. 14 (2014) 416—422.
[19] J.P. Huang, D.D. Yuan, H.Z. Zhang, Y.L. Cao, G.R. Li, H.X. Yang, X.P. Gao, RSC Adv. 3 (2013) 12593—12597.
[20] X. Gu, L.J. Li, Y. Wang, P.C. Dai, H.B. Wang, X.B. Zhao, Electrochim. Acta 211 (2016) 77—82.
[21] G.Y. Zhang, C.X. Chu, J. Yang, C.H. Tung, Y.F. Wang, J. Phys. Chem. C 123 (2019) 7025—7032.
[22] D.W. Su, S.X. Dou, G.X. Wang, Chem. Mater. 27 (2015) 6022—6029.
[23] F. Bella, A.B. Munoz-Garcia, G. Meligrana, A. Lamberti, M. Destro, M. Pavone, C. Gerbaldi, Nano Res. 10 (2017) 2891—2903.
[24] S. Liu, J.K. Feng, X.F. Bian, J. Liu, H. Xu, Energy Environ. Sci. 9 (2016) 1229—1236.
[25] S. Auvinen, M. Alatalo, H. Haario, J.P. Jalava, R.J. Lamminmaki, J. Phys. Chem. C 115 (2011) 8484—8493.
[26] S.W. Park, J.T. Jang, J. Cheon, H.H. Lee, D.R. Lee, Y. Lee, J. Phys. Chem. C 112 (2008) 9627—9631.
[27] M.A.S. de Abreu, E. Morgado, P.M. Jardim, B.A. Marinkovic, Cent. Eur. J. Chem. 10 (2012) 1183—1198.
[28] C. Perego, R. Revel, O. Durupthy, S. Cassaignon, J.P. Jolivet, Solid State Sci. 12 (2010) 989—995.
[29] Y.M. Lin, P.R. Abel, D.W. Flaherty, J. Wu, K.J. Stevenson, A. Heller, C.B. Mullins, J. Phys. Chem. C 115 (2011) 2585—2591.
[30] J.N. Tiwari, R.N. Tiwari, K.S. Kim, Prog. Mater. Sci. 57 (2012) 724—803.
[31] N. Li, Q. Zhang, J.B. Joo, Z.D. Lu, M. Dahl, Y. Gan, Y.D. Yin, Nanoscale 8 (2016) 9113—9117.
[32] B.H. Toby, R.B. Von Dreele, J. Appl. Crystallogr. 46 (2013) 544—549.
[33] P. Juhas, T. Davis, C.L. Farrow, S.J.L. Billinge, J. Appl. Crystallogr. 46 (2013) 560—566.
[34] C.J. Howard, T.M. Sabine, F. Dickson, Acta Crystallogr. B 47 (1991) 462—468.
[35] P. Scherrer, Nachr. Ges. Wiss. Goettingen, Math.-Phys. Kl. 1918 (1918) 98—100.
[36] W.F. Zhang, Y.L. He, M.S. Zhang, Z. Yin, Q. Chen, J. Phys. D Appl. Phys. 33 (2000) 912—916.
[37] U. Balachandran, N.G. Eror, J. Solid State Chem. 42 (1982) 276—282.
[38] C.F. Liu, Z.G. Neale, G.Z. Cao, Mater. Today 19 (2016) 109—123.
[39] J. Chen, Y. Zhang, G.Q. Zou, Z.D. Huang, S.M. Li, H.X. Liao, J.F. Wang, H.S. Hou, X.B. Ji, Small 12 (2016) 5554—5563.
[40] J. Wang, J. Polleux, J. Lim, B. Dunn, J. Phys. Chem. C 111 (2007) 14925—14931.
[41] B.E. Conway, V. Birss, J. Wojtowicz, J. Power Sources 66 (1997) 1—14.
[42] H. Lindstrom, S. Sodergren, A. Solbrand, H. Rensmo, J. Hjelm, A. Hagfeldt, S.E. Lindquist, J. Phys. Chem. B 101 (1997) 7717—7722.
[43] C.J. Deng, M.L. Lau, H.M. Barkholtz, H.P. Xu, R. Parrish, M. Xu, T. Xu, Y.Z. Liu, H. Wang, J.G. Connell, K.A. Smith, H. Xiong, Nanoscale 9 (2017) 10757—10763.
[44] V. Petkov, Mater. Today 11 (2008) 28—38.
[45] S.J.L. Billinge, M.G. Kanatzidis, Chem. Commun. (2004) 749—760.
[46] M. Fernandez-Garcia, C. Belver, J.C. Hanson, X. Wang, J.A. Rodriguez, J. Am. Chem. Soc. 129 (2007) 13604—13612.
[47] J.A. Dawson, J. Robertson, J. Phys. Chem. C 120 (2016) 22910—22917.
[48] M. Madian, A. Eychmuller, L. Giebeler, Batteries-Basel (2018) 4.